Zahn, R., Comas, M.C., and Klaus, A. (Eds.), 1999
Proceedings of the Ocean Drilling Program, Scientific Results, Vol. 161

24. STRUCTURE AND TECTONIC STRESSES IN METAMORPHIC BASEMENT, SITE 976, ALBORAN SEA[1]

François Dominique de Larouzière,[2,3] Philippe A. Pezard,[2,4] Maria C. Comas,[5] Bernard Célérier,[6] and Christophe Vergniault[2]

ABSTRACT

A complete set of downhole measurements, including Formation MicroScanner (FMS) high-resolution electrical images and BoreHole TeleViewer (BHTV) acoustic images of the borehole wall were recorded for the metamorphic basement section penetrated in Hole 976B during Ocean Drilling Program Leg 161. Because of the poor core recovery in basement (under 20%), the data and images obtained in Hole 976B are essential to understand the structural and tectonic context wherein this basement hole was drilled. The downhole measurements and high-resolution images are analyzed here in terms of structure and dynamics of the penetrated section.

Electrical resistivity and neutron porosity measurements show a generally fractured and consequently porous basement. The basement nature can be determined on the basis of recovered sections from the natural radioactivity and photoelectric factor. Individual fractures are identified and mapped from FMS electrical images, providing both the geometry and distribution of plane features cut by the hole. The fracture density increases in sections interpreted as faulted intervals from standard logs and hole-size measurements. Such intensively fractured sections are more common in the upper 120 m of basement. While shallow gneissic foliations tend to dip to the west, steep fractures are mostly east dipping throughout the penetrated section.

Hole ellipticity is rare and appears to be mostly drilling-related and associated with changes in hole trajectory in the upper basement schists. In the gneisses, a very slight short-axis ellipticity pointing steadily N035° is obtained. A few narrow intervals with sharp changes in hole geometry are also identified from mechanical calipers in lower basement. These sections are found to correspond to active faults from BHTV images. The analysis of an 80-m-long basement interval reveals the presence of 20 active faults. The mapping of each fault plane and drilling-induced slip vector leads to the identification of an extensional tectonic regime, with the minimum stress axis S_3 pointing N080°. Assuming a near vertical maximum stress direction (S_1; about 33 MPa at 800 mbsf), and that pore pressure (P_o) equals lithostatic pressure (S_o), the magnitude of the three principal stresses can be determined as a function of the friction coefficient (μ). As Hole 976B is located in the western part of the Alboran Basin, this new result indicates a present-day N080° directed extensional or transtensional stress component. This result is compatible with the actual kinematics of Europe-Africa plate convergence in the westernmost Mediterranean.

INTRODUCTION

The Alboran Sea is considered as an extensional basin located in a collisional setting. The basin is rimmed by orogenic cordilleras (Betic Chain in southeastern Spain, Rif in Morocco). One of the objectives for Ocean Drilling Program (ODP) Leg 161 was to obtain samples of basement lithology in the western Mediterranean, as well as to identify the tectonic characteristics of this basement. Site 976 is located on a structural high within the southern Spanish margin, off Malaga, and close to Deep Sea Drilling Project (DSDP) Site 121. After drilling through a thick Pleistocene and Miocene sedimentary sequence, the basement was perforated at Site 976 in Holes B and E, and the first direct evidence of a metamorphic lithology in this area was obtained.

This paper is focused on the study of basement structures penetrated in Hole 976B, where a full set of downhole data (standard logs) and images (Formation MicroScanner [FMS] and BoreHole TeleViewer [BHTV]) was recorded. Basement was reached at 669.7 meters below seafloor (mbsf), and the hole terminated at 928.7 mbsf. Because of the hard-rock lithology and the presence of numerous breccias and faults, the total core recovery was rather low, averaging 19% in this metamorphic interval (Fig. 1). The dip of the main foliation planes was determined on board ship, but the dip direction of these planes is unknown from cores that were not oriented.

Core Analysis and Lithostratigraphy

The basement lithology derived from core in Hole 976B may be divided in two main units (Fig. 1): (1) from 669.7 down to 794.0 mbsf, dark gray high-grade micaschists (quartz-biotite-sillimanite-plagioclase), within which layers of calcite and dolomite marble are interbedded (Comas, Zahn, Klaus, et al., 1996); (2) below 794.0 mbsf, the recovered samples consist of medium gray massive high-grade metasedimentary gneissic rocks (quartz-biotite-sillimanite), with local migmatitic facies. Leucogranitic material (quartz, feldspar, plagioclase, and cordierite) was found episodically, probably occurring as small bodies or dikes cross-cutting the metamorphic series. Numerous zones of thick breccias were encountered for example at 677.0, 705.0, 750.0, 765.0, and 913.0 mbsf. In Hole 976E, the basement was reached at 652.1 mbsf and the hole ends at 736.3 mbsf. Despite the fact that the two holes 976B and 976E are very close to one another (about 20 m apart), the lithologic units are quite different, evidence of the presence of subvertical structures.

Downhole Geophysical Measurements

Downhole measurements were recorded in both basement holes, but operational difficulties prevented the recording of data and images through the sediment/basement contact in Hole 976B, and borehole wall images in Hole 976E (Fig. 2). The electrical resistivity profile obtained in Hole 976E images a sharp, probably recently faulted

[1]Zahn, R., Comas, M.C., and Klaus, A. (Eds.), 1999. *Proc. ODP, Sci. Results,* 161: College Station, TX (Ocean Drilling Program).

[2]Laboratoire de Mesures en Forage, ODP-NEB, BP 72, F-13545 Aix-en-Provence cedex 20, France.
[3]GAÏA, 16 boulevard Notre-Dame, F-13006 Marseille, France. gaia@lac2.gulliver.fr
[4]Pétrologie Magmatique, CEREGE (FU 17 du CNRS), BP 80, F-13545 Aix-en-Provence cedex 4, France.
[5]Instituto Andaluz de Ciencias de la Tierra, Universidad de Granada, Campus Fuentenueva, E-18002, Granada, Spain.
[6]Université de Montpellier II-CNRS (UMR 5569), cc 57, F-34095 Montpellier cedex 5, France.

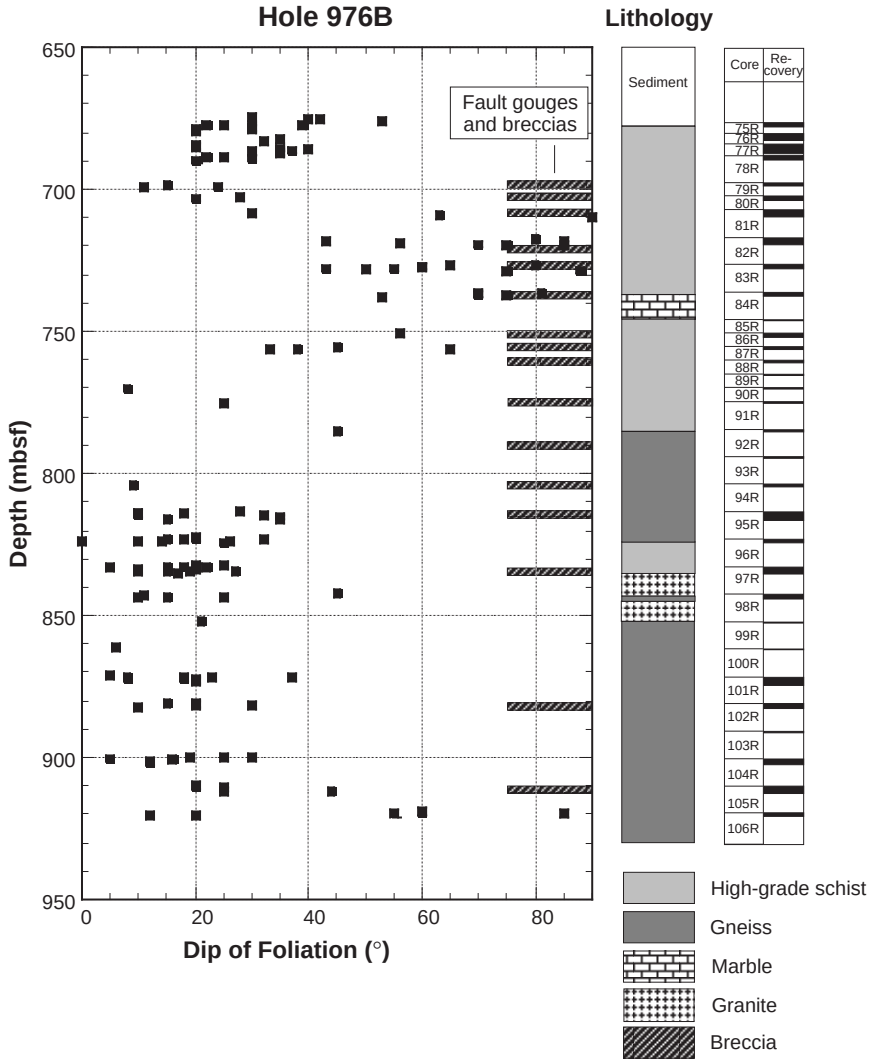

Figure 1. Structural dip of foliation mapped from core in the basement section of Hole 976B. Main lithotypes, occurrences of fault gouges and breccias, and core recovery are indicated to the right.

basement/sediment contact. The electrical resistivity measurement magnitude in the sediment and basement however is comparable in the two holes. A full suite of logging tools from Schlumberger was run into the accessible basement section of Hole 976B, from 700.0 to 900.0 mbsf. This suite included the "quad" combination of geophysical sensors, the FMS electrical imager, the geochemical tool (GLT), and the BHTV acoustic imager.

Hole 976B conditions were found to be better in the lower part of this basement section where gneisses were sampled (Fig. 3). While the hole shape is close to the bit size (9.875 in) over this interval, it is generally much larger above 800.0 mbsf, in the schists. The hole deviation from vertical remains under 7° (Fig. 3), with sharp changes in front of large hole and high neutron-porosity intervals. These short intervals are often the site of natural radioactivity and photoelectric factor (P_{ef}) decrease (e.g., 718, 783, 808, 828, and 833 mbsf; Fig. 3), and can be associated with the presence of fault gouges and breccias (Fig. 1). Other intervals with low radioactivity, high Th/U ratio, but not necessarily high neutron-porosity or caliper-size changes (e.g., 812 and 858 mbsf) point at probably older features, not necessarily active at present.

DOWNHOLE ELECTRICAL IMAGES

FMS Sensor and Image Processing

The FMS creates a picture of the borehole wall by mapping the electrical conductivity using an array of small, pad-mounted electrodes (Ekstrom et al., 1987; Lüthi and Banavar, 1988). The slimhole configuration developed for ODP uses four pads, each with 16 buttons. A single pass of the tool maps about 22 percent of the borehole surface in a 25.4-cm-diameter (10 in) borehole. Each electrode is oriented in space with 3-axes accelerometers and fluxgate magnetometers, making it possible to derive the strike and dip of geological structures. Because of electrode geometry, the tool has a moderate depth of investigation (a few centimeters). While FMS data are recorded every 2.5 mm as the tool moves up the borehole, the vertical resolution of individual features is on the order of 1.0 cm.

The tool can, however, detect thinner features provided that they have a sufficient resistivity contrast with the surrounding matrix. The images recorded with the FMS show electrical conductivity changes, particularly those resulting from beds different in nature, as well as the presence of fractures, either open or mineralized. Data processing (using Logos software of Schlumberger) is required to convert the raw data into a grayscale (or color scale) image representative of conductivity changes in the rock. Data processing includes conversion of the current intensity to variable-intensity gray or color images, then to an electrical conductivity map of the borehole surface. In the former, black corresponds to higher conductivity, and white corresponds to lower values.

FMS Data and Image Analysis

The FMS images recorded in Hole 976B (Fig. 4) were analyzed on a workstation using FracView, a Schlumberger interpretative soft-

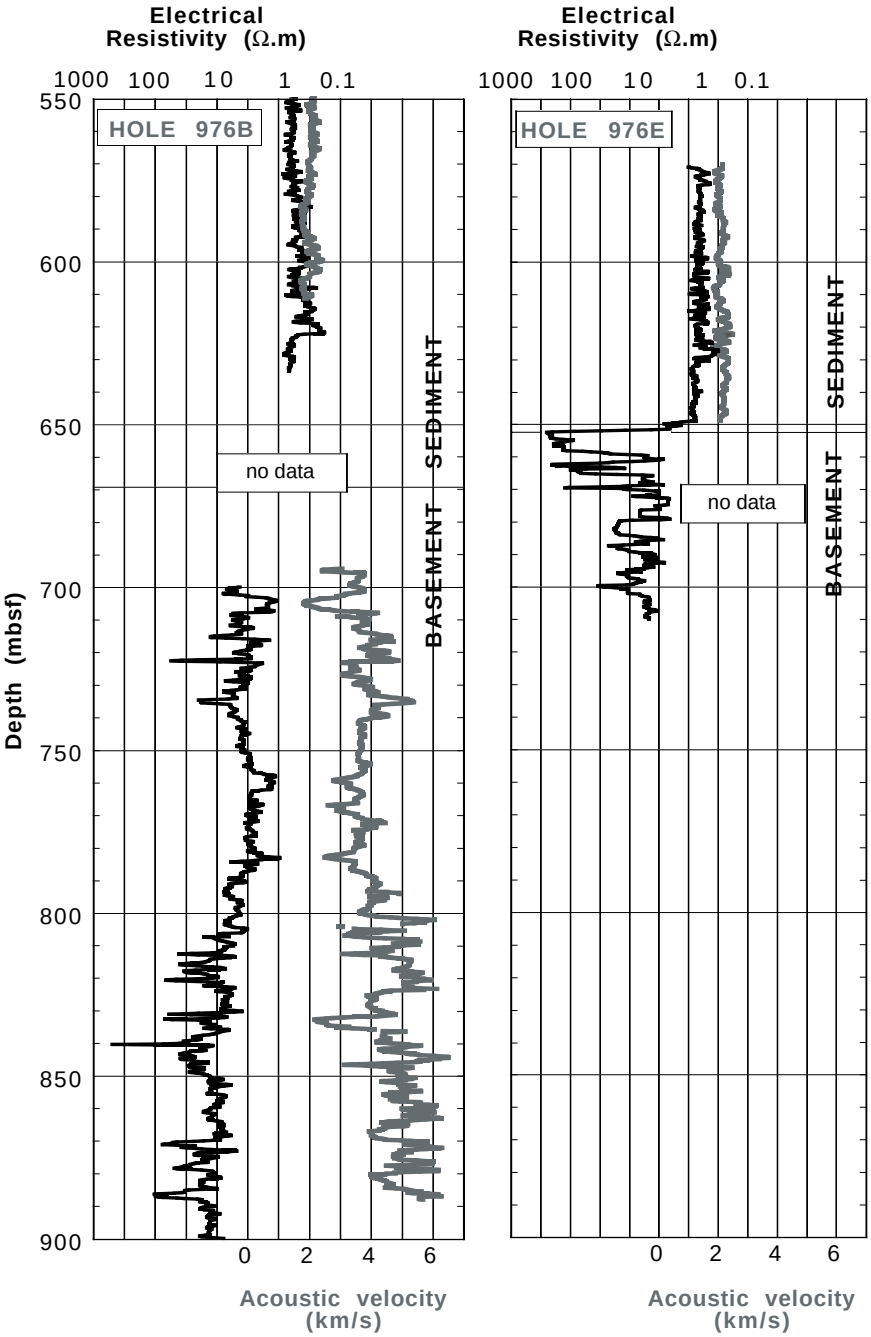

Figure 2. Physical properties of the sediment/basement transition at Site 976. Black curve = resistivity, gray curve = acoustic velocity. **Left:** Hole 976B, no data were acquired in the transition between basement and sedimentary cover because of bad hole conditions. The basement measurements were made as the pipe was lowered to 680 mbsf. **Right:** Hole 976E, the electrical resistivity profile images a sharp, probably recently faulted contact. The measurement magnitudes in the sediment and basement are comparable in the two holes.

ware for the interactive display and analysis of oriented images. The fracture analysis method used in FracView is presented in Lüthi and Souhaité (1990) and, beyond detection and mapping, is aimed at providing a quantitative evaluation of the "fracture aperture" from electrical images of the borehole surface. Mapping fractures from FMS images consists of finding sinusoidal traces showing a conductivity contrast with the surrounding rock. Any plane intersected by a cylindrical borehole is in fact represented as a sinusoid on a depth-azimuth plot. The dip angle is related to the amplitude of the sinusoid, and the dip direction (or plunge) is given by the lowermost point of the trace. Such a sinusoidal pattern is provided by a 20-cm-thick, electrically conductive fault zone dipping south at about 873 mbsf. This outstanding event is detected also with neutron porosity, photoelectric effect, and Th/U ratio profiles (Fig. 3), and is surrounded by shallower and electrically less conductive structures corresponding to the foliation planes of the gneiss. Each plane was mapped individually on a workstation with FracView and then identified with a blue trace (Fig. 4).

Planes totaling 1600 were mapped from FMS images in metamorphic basement, and are then presented as "tadpoles" and dip directions (Fig. 5). The quality of the mapping decreases where the hole size becomes too large, as between 780 and 790 mbsf, for example. As predicted from the mapping of foliation planes from core (Fig. 1), subhorizontal structures are more numerous in the lower part of the hole, where a general dip of these shallow planes to the south is seen (Fig. 5). Steeper features with dip angles larger than 60° tend to plunge to the east (Fig. 6), in an opposite direction from most of the foliation planes.

In this context, variations in hole shape and size might be used to determine the direction of the minimum horizontal stress direction, using the direction of borehole long axis (Bell and Gough, 1979; Mastin et al., 1991; Plumb and Hickman, 1985; and many others). In

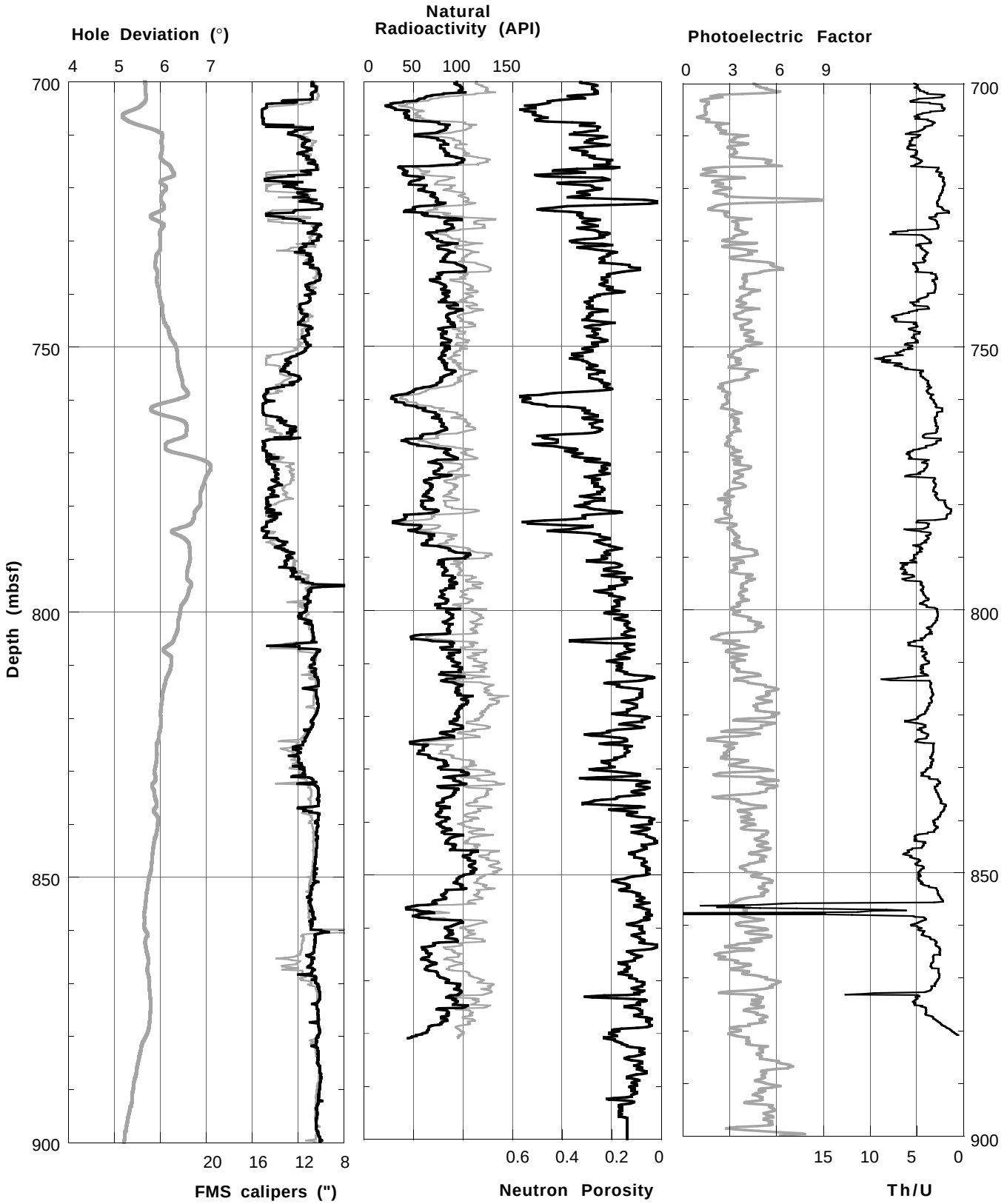

Figure 3. Composite log of geophysical and hole-related measurements recorded in Hole 976B. **Left:** Hole deviation with respect to vertical, in gray, and orthogonal FMS calipers. **Center:** Natural radioactivity (SGR in grey, and CGR in black) and neutron porosity. **Right:** Photoelectric factor in gray, and Th/U ratio. The hole slightly deviates to the west.

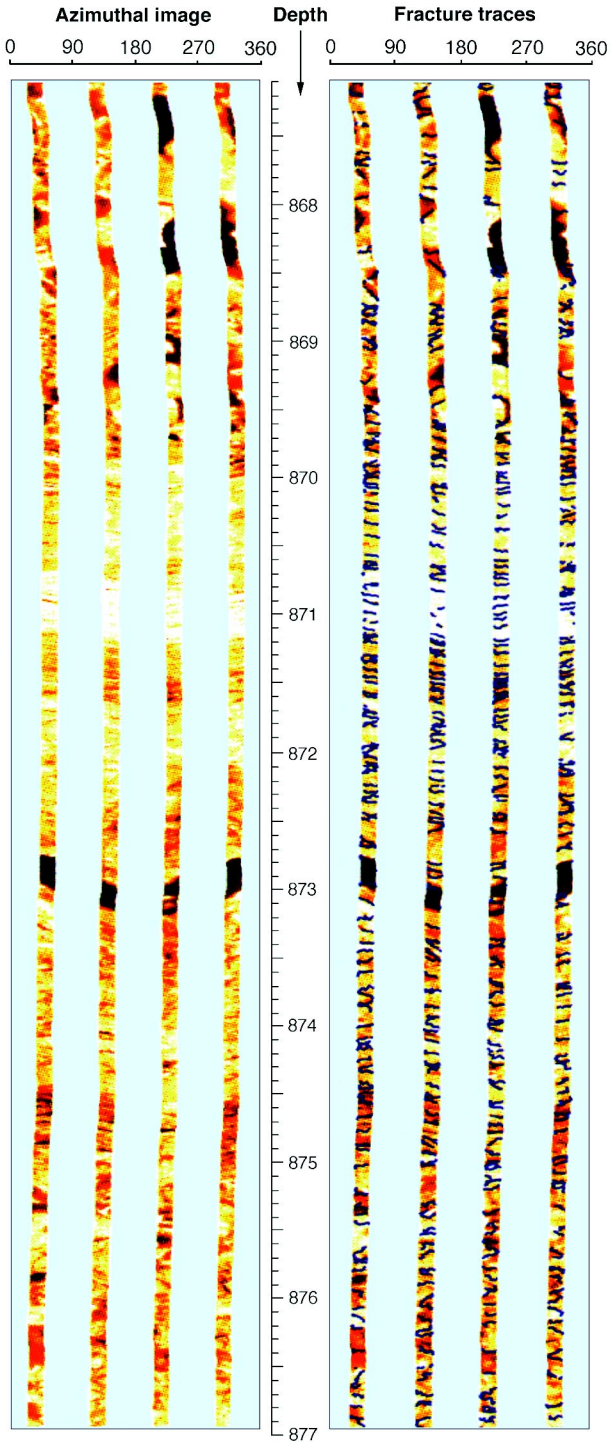

Figure 4. Example of FMS image recorded in Hole 976B (depth interval: 867.0–877.0 mbsf). **Left:** Azimuthal image oriented with respect to geographical north, with foliation and fracture traces. **Right:** Fracture and foliation traces (outlined in blue) mapped individually with FracView. A fault trace dipping generally to the south is identified at 873.0 mbsf. This trace corresponds to a neutron porosity increase, low Pef values and a high Th/U ratio (Fig. 3).

order to evaluate the potential development of hole ellipticity caused by pipe wear, the hole short-axis direction is presented here with a curve corresponding to the hole azimuth (HAZI) plus 90° (Fig. 7; top). The two directions should overlay in the case of pipe-induced wear, which appears to be the case in a statistical sense from 700 to 790 mbsf. As expected in such a situation, the fit is particularly good in sections with sharp changes in hole deviation (760 to 790 mbsf). In the lower part of the hole, the very steady direction of hole ellipticity does not appear to be related to pipe wear.

DOWNHOLE ACOUSTIC IMAGES

BHTV Downhole Sensor

The digital BHTV from Schlumberger called UBI for "Ultrasonic Borehole Imager" was also used during ODP Leg 161 in Hole 976B. The UBI sensor transmits acoustic pulses from the tool to the borehole wall and back more than a hundred times per rotation around the hole. The amplitude and travel time of each acoustic pulse reflected from the borehole wall is recorded, then assembled into high-resolution images of the borehole wall (Fig. 8). The reflected impulse contains information about the geometry of the borehole in the travel time and about the reflectivity of the borehole wall in the amplitude of the pulse. A detailed technical description of the digital BHTV and the set-up of the BHTV recording system used by ODP is given in Comas, Zahn, Klaus, et al. (1996).

BHTV Image Analysis

Stress-induced borehole deformations can be detected from the acoustic images of a borehole surface in deep holes (Bell and Gough, 1979; Barton, 1988; and many others). More recent studies have shown that stress release along active fault planes caused by drilling can be the source of changes in hole shape (Héliot et al, 1989; Maury and Sauzay, 1989; Maury and Zurdo, 1996). A substantial hole size reduction is obtained, for example, in the case of a compressive rupture (Fig. 9). However, the theoretical shapes presented in Figure 9 are not necessarily obtained from acoustic images, but are mainly caused by back-reaming of the drill pipe on the way out of the hole, often within the footwall section. As a result, enlarged borehole cross sections are obtained, as in Hole 976B (808.4 mbsf) where a sinistral strike-slip rupture is detected (Fig. 10). Subsequent reaming on the south side of the hole is inferred from the cross section. Opposite sides of the borehole may be mapped to determine the offset between centers, which corresponds to the projection of the slip vector in the plane orthogonal to the borehole axis. A slight extensional component is also detected at 808.4 mbsf, while a purely extensional shape is imaged at 865.1 mbsf (Fig. 10).

Such sharp changes in borehole shape are present in the mechanical caliper record and may be outlined with the first derivative of any of the caliper readings (Fig. 11). Large values of this curve are often correlated to high electrical conductivity values and, less frequently, low natural radioactivity records (Fig. 11; 825, 858, and 873 mbsf). The detailed borehole cross sections extracted from BHTV acoustic images were investigated on the basis of this first derivative in order to determine the presence of active faults. A total of 20 faults was obtained (Table 1) between 820 and 880 mbsf in Hole 976B. In each case, the fault plane was mapped from the BHTV amplitude image, and the slip vector obtained from the analysis of disrupted sections. For each fault, 5 to 11 measurements were made at nearby levels to compute the slip direction and magnitude. Most of the faults analyzed over 60 m in Hole 976B (820 to 880 mbsf) were found to slip according to a normal mode of deformation (Table 1).

STRESS FIELD ANALYSIS

Drilling-Induced Faulting in Basement

The fault and slip data extracted from the interval 820.0–880.0 mbsf were inverted in terms of stress tensor orientation and aspect ratio using a method similar to those proposed by Carey and Brunier

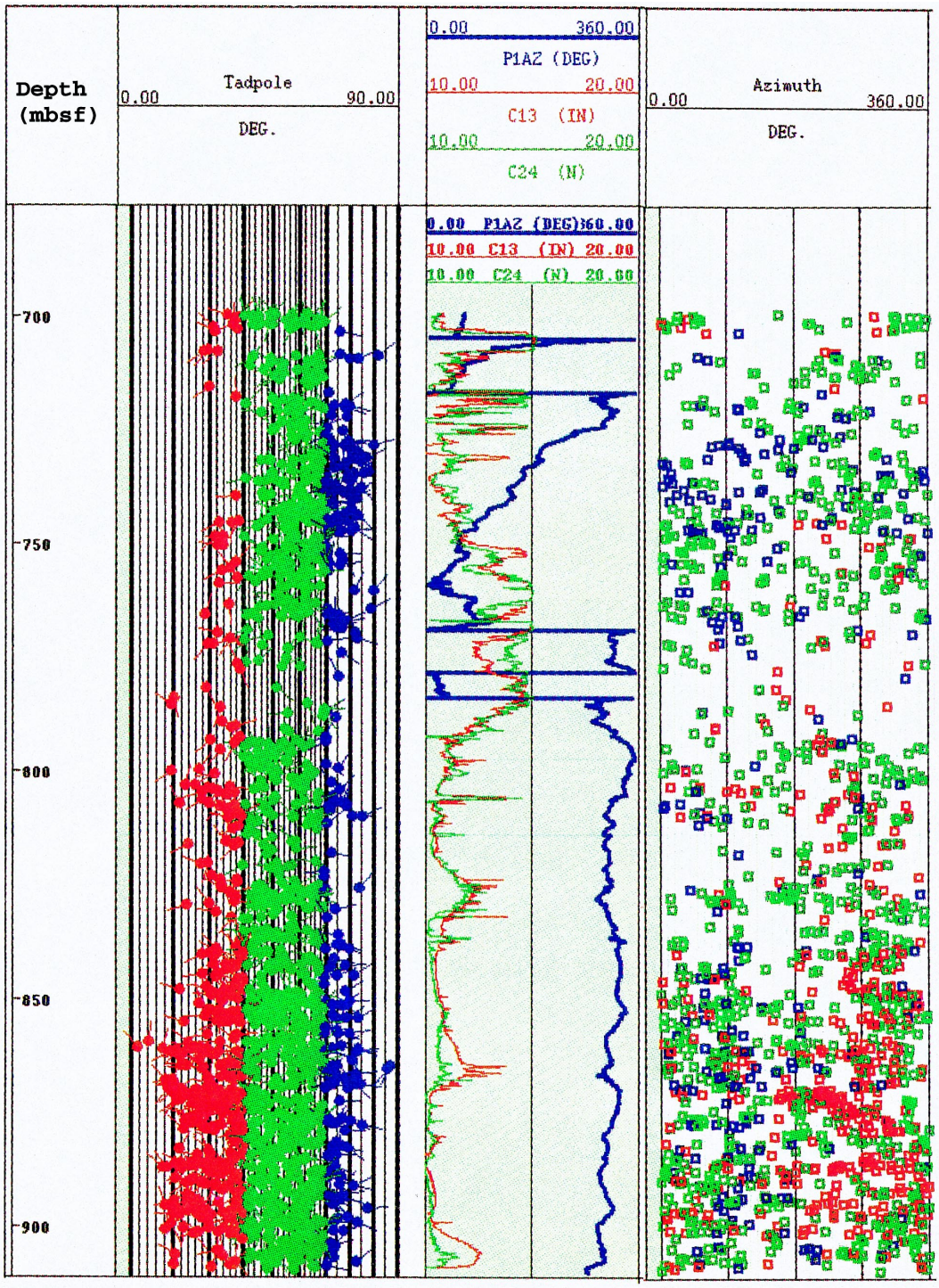

Figure 5. Summary of results from FMS image analysis in Hole 976B, using FracView. **Left:** Depth below seafloor (left) associated with the 1600 individual conductive events mapped from FMS images and presented in terms of dip angle and azimuth as a "tadpole." The planes are here presented in three sets with respect to dip angle: horizontal (0°–30°; red), intermediate (30°–60°; green), and steep (60°–90°; blue). **Center:** Orientation with respect to north of pad #1 of the FMS tool into the hole represented as P1AZ. Orthogonal calipers (C13 and C24) describe the variations in borehole size, outlining the presence of fault zones with large values. **Right:** Summary of the 1600 planes mapped presented in terms of dip direction. The lower density of planes mapped between 770.0 and 780.0 mbsf is locally a result of poor image quality related to large hole size.

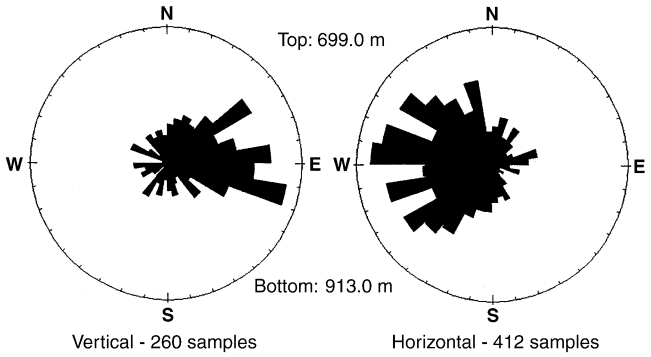

Figure 6. Rose diagrams of dip directions for near-vertical (**left**) and near-horizontal (**right**) planes derived from FMS image mapping in Hole 976B.

(1974), Armijo and Cisternas (1978), Angelier (1979), and Etchecopar et al. (1981), with additional developments (Célérier, 1988, 1995; Tajima and Célérier, 1989). In all, 60% of the slip orientations can be reconciled with a N080° trending extensional stress field (Fig. 12), with S_1 slightly tilted to the South and a stress ratio equal to:

$$(S_1 - S_2) / (S_1 - S_3)] = 0.41. \quad (1)$$

Frictional Limit of the Crust

S_1 can be evaluated at 800 mbsf, for example, from the lithostatic charge to obtain 33.0 (± 2.0) MPa, which places bounds on the two horizontal components of the stress tensor. With a hydrostatic charge (S_e) equal to about 19.0 MPa at this depth, stresses within the Alboran Sea basement might be estimated using the frictional limit of the crust proposed by Sibson (1974) or Brace and Kohlstedt (1980). A relation between maximum (S_1), and minimum (S_3) principal stresses and pore pressure (P_e) proposed by Jaeger and Cook (1977) was used successfully by Moos and Morin (1991), for example, as well as others. The near verticality of the borehole in the analyzed section with a deviation generally less than 7° (Fig. 7), and the S_1 direction determined from active faulting (Zoback et al., 1989), establishes the validity of this model for the present analysis. The friction law is expressed as:

$$[(S_1 - P_e) / (S_3 - P_e)] = \alpha, \text{ where } \alpha = [(1 + \mu^2)^{1/2} + \mu]^2, \quad (2)$$

where μ is referred to as the friction coefficient.

If the pore pressure in the basement is considered to be hydrostatic ($P_e = S_e = 19$ MPa), and S_1 lithostatic ($S_1 = 33$ MPa near the base of the hole), a simplified relationship is obtained with:

$$S_3 = 19 + (14 / \alpha), \quad (3)$$

and S_2 can be computed from (1) and (3) accordingly.

Compressive Ruptures of the Borehole Surface

In the lower part of the basement, the direction of the hole short-axis is found to be extremely stable in azimuth, as revealed from mechanical calipers orientation (Figs. 5, 7). The differences between the two FMS caliper readings remains, however, extremely small (under 0.1 in). This difference rarely exceeds 0.8 in (Fig. 7), except in faulted intervals (830 to 840, 860 to 870, and 900 to 910 mbsf). The process of faulting, and subsequent alteration from fluid circulation, apparently reduces locally the mechanical strength of the formation to allow for the larger size ruptures in the direct vicinity of faults (Figs. 5, 7).

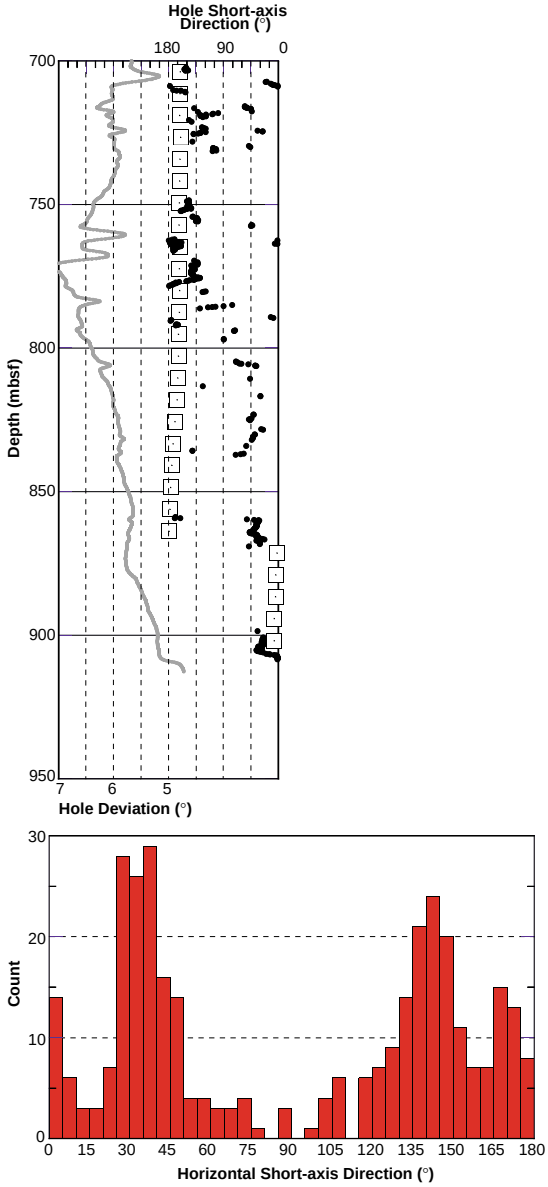

Figure 7. **Top:** Hole short-axis direction presented against hole deviation (gray) derived from the orientation module of the FMS sensor. The black dots indicate hole sections with caliper-reading differences larger than 0.8 in. The continuous trace of open squares is pointing in the borehole azimuth direction plus 90°. In the case of hole elongation caused by pipe wear, this continuous trace and the dots should align. **Bottom:** Histogram of hole short-axis azimuth, with two maxima pointing N140° for upper basement schists, and N035° for lower basement gneisses.

Borehole wall failures leading to the development of hole ellipticity are often analyzed in terms of compressive rupture of the borehole surface (Bell and Gough, 1979; Barton, 1988; Moos and Zoback, 1990). If present in Hole 976B, which could be inferred from the stable orientation of the FMS tool in the hole and in spite of detectable ellipticity from mechanical calipers, compressive ruptures of the borehole surface must be very limited in extension. In any case, if present, these ruptures must be smaller than the size of the FMS pad (7 cm wide), although sufficient to guide the downhole sensor along more than 100 m.

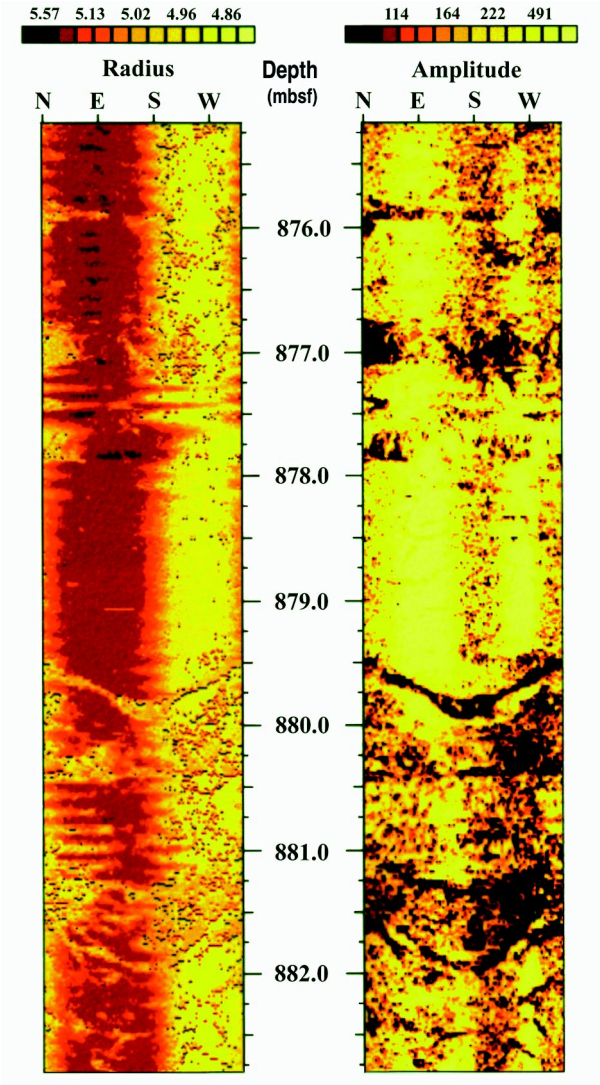

Figure 8. Examples of BHTV images over 8 m of basement in Hole 976B. **Left:** Transit time converted to a borehole radius image. **Right:** Amplitude image of BHTV reflected wavetrains.

While a direct determination of horizontal stress direction from hole ellipticity would here point N125° for S_3, the analysis of drilling-induced faulting has previously determined a very different direction (N080°). This difference might arise from a substantial degree of mechanical anisotropy of the metamorphic rocks cored over this interval, yielding ruptures misaligned with principal stresses, as found in the KTB deep continental drilling in a geologically similar formations (Mastin et al., 1991). The slight but consistently aligned ruptures of the borehole surface from 800 mbsf to the bottom of the hole could imply that the compressive strength of the rock is here close to the limit of rupture. We may consequently equal there the maximum horizontal circumferential stress ($\sigma_{\theta\theta}$) to the compressive strength (C_0) with (Zoback et al., 1985):

$$[3\ S_2 - S_3 - 2\ P_e]\ \#\ C_0. \quad (4)$$

The knowledge of C_0 may then lead to another evaluation of S_2 and S_3 (Moos and Morin, 1991) as a function of μ, combining equations (1), (2), and (4). C_0 may also be estimated from (3) and (4) with:

$$C_0 = (2.8) \cdot [(9 + 1/\alpha)]. \quad (5)$$

leading to a very narrow range of values for C_0 (25.8 to 27.3 MPa; Fig. 13) over a wide range of friction coefficients (μ). The values of

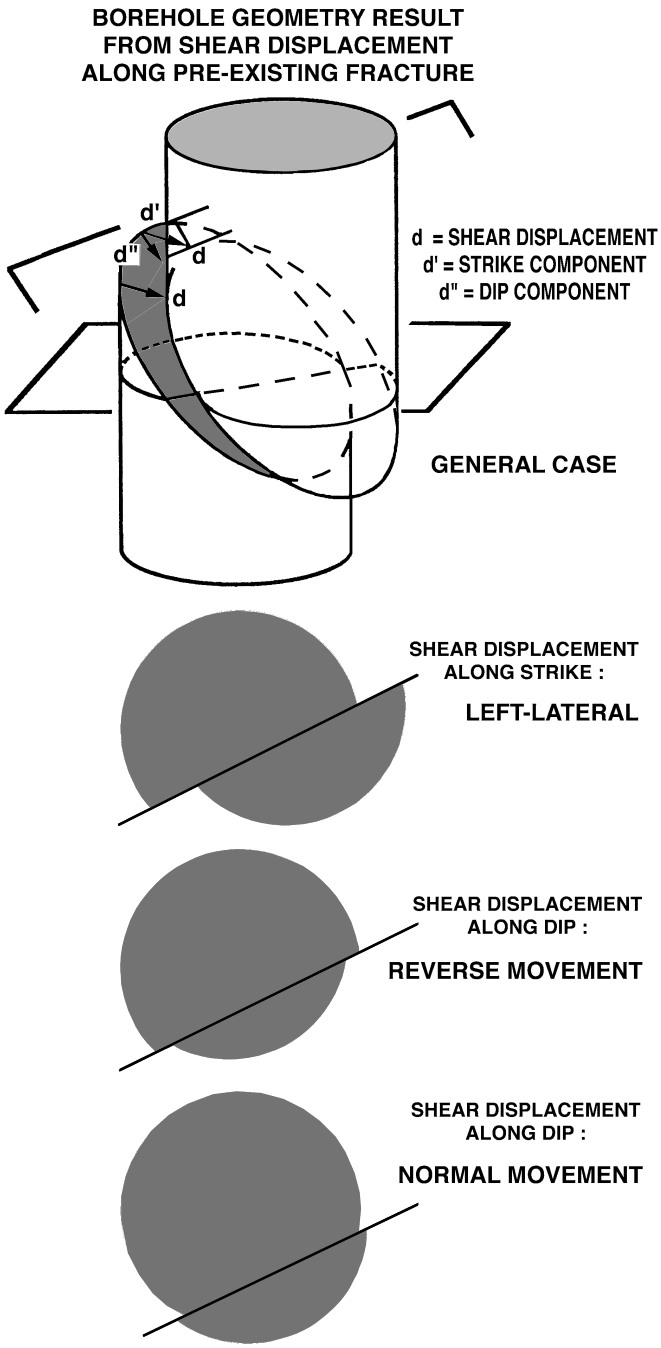

Figure 9. Sketch of the three possible modes of deformation of the borehole section caused by shearing along active fault planes identified from BHTV transit time data (after Maury and Zurdo, 1996).

μ under 0.40–0.50 would correspond to the presence of very weak faults. The large number of extensional to strike-slip ruptures mapped from acoustic images advocates here for a very low difference between components of the stress field, hence from Figure 13 for the lower range of values of friction coefficient (μ) where differential stresses are lower.

CONCLUSION

Site 976 was the first site of Leg 161 to address the tectonic objectives of the drilling campaign. Hole 976B penetrated 267.0 m into

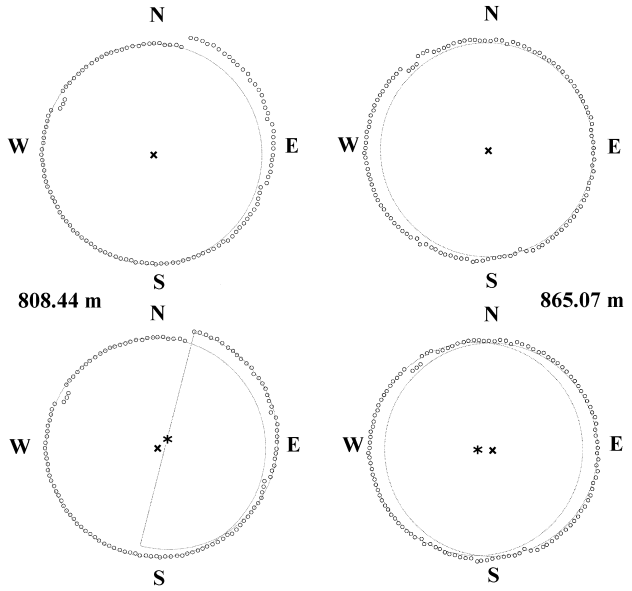

Figure 10. Examples of hole shearing caused by stress release along two active faults from the basement of Hole 976B. **Left:** Sinistral transtensive strike-slip faulting, trending N010° at 808.4 mbsf. **Right:** Purely extensive east-west–trending slip along a north-south–striking fault, pointing at a N090° minimum horizontal stress direction. Note that only part of the expected shape is obtained as a result of reaming from the drill pipe on the way out of the hole.

high-temperature metamorphic basement with well-developed foliations. The main lithologic units identified in the core are recognized in downhole measurements and high-resolution borehole wall images, allowing us to extend the lithologic description over missing intervals (about 80% of the section). Azimuths of foliation planes and tectonic structures are obtained from FMS image analyses. As images are oriented in space with respect to true north, an analysis of the dip directions of the detected events can be obtained, which is not possible with nonoriented cores.

This study provides a first draft of the structural environment within which these metamorphic rocks have evolved. FMS and BHTV images reveal that low-angle foliation planes are mainly dipping to the west. The most fractured part of the basement is in the upper 100 m, with steep planes dipping to the east. The ruptures identified and mapped in the 820.0 to 880.0 mbsf interval are coherent with the presence of an extensional to transtensive strike-slip stress regime at this site, with S_3 trending in a N080° direction. As Hole 976B is located in the western part of the Alboran Basin, this new result indicates a present-day N080° directed extensional or transtensional stress component. This result is compatible with the actual kinematics of Europe-Africa plate convergence in the westernmost Mediterranean.

ACKNOWLEDGMENTS

We thank Dan Moos for a thoughtful constructive review of the manuscript. We also thank Schlumberger for making available the "FracView" FMS analysis software, and GAIA Entreprise for giving access to "FastDyn", a code for BHTV and stress field analysis. This work was supported by the "Marine Geosciences" ODP support program of CNRS, France.

REFERENCES

Angelier, J., 1979. Determination of the mean principal directions of stresses for a given fault population. *Tectonophysics*, 56:T17–T26.

Armijo, R., and Cisternas, A., 1978. Un problème inverse en microtectonique cassante. *C. R. Acad. Sci. Ser. 2*, 287:595–598.

Barton, C.A., 1988. Development of in-situ stress measurement techniques for deep drillholes [Ph.D. dissert.]. Stanford Univ., Stanford, CA.

Bell, J.S., and Gough, D.I., 1979. Northeast-southwest compressive stress in Alberta: evidence from oil wells. *Earth Planet. Sci. Lett.*, 45:475–482.

Brace, W.F., and Kohlstedt, D.L., 1980. Limits on lithospheric stress imposed by laboratory experiments. *J. Geophys. Res.*, 85:6248–6252.

Carey, E., and Brunier, B., 1974. Analyse théorique et numérique d'un modèle mécanique élémentaire appliqué à l'étude d'une population de failles. *C. R. Acad. Sci. Ser. D*, 279:891–894.

Célérier, B., 1988. How much does slip on reactivated fault plane constrain the stress tensor? *Tectonics*, 7:1257–1278.

————, 1995. Tectonic regime and slip orientation of reactivated faults. *Geophys. J. Int.*, 121:143–191.

Comas, M.C., Zahn, R., Klaus, A., et al., 1996. *Proc. ODP, Init. Repts.*, 161: College Station, TX (Ocean Drilling Program).

Ekstrom, M.P., Dahan, C., Chen, M.-Y., Lloyd, P., and Rossi, D.J., 1987. Formation imaging with microelectrical scanning arrays. *Log Analyst*, 28:294–306.

Etchecopar, A., Vasseur, G., and Daignières, M., 1981. An inverse problem in microtectonics for the determination of the stress tensor from fault striation analysis. *J. Struct. Geol.*, 3:51–65.

Héliot, D., Etchecopar, A., and Cheung, P., 1989. New developments in fracture characterisation from logs. *In* Maury, V., and Fourmaintraux, D. (Eds.), *Rock at Great Depth: Rock Mechanics and Rock Physics at Great Depth:* Rotterdam (Balkema), 3:1471–1478.

Jaeger, J.C., and Cook, N.G.W., 1977. *Fundamentals of Rock Mechanics:* New York (Chapman and Hall).

Lüthi, S.M., and Banavar, J.R., 1988. Application of borehole images to three-dimensional geometric modeling of eolian sandstone reservoirs, Permian Rotliegende, North Sea. *AAPG Bull.*, 72:1074–1089.

Lüthi, S.M., and Souhaité, P., 1990. A method for fracture extraction and width determination from electrical borehole scans. *Geophysics*, 55:821–833.

Mastin, L.G., Heinemann, B., Krammer, A., Fuchs, K., and Zoback, M.D., 1991. Stress orientation in the KTB pilot hole determined from wellbore breakouts. *Sci. Drill.*, 2:1–12.

Maury, V.M., and Sauzay, J.-M., 1989. Rupture de puits provoquée par glissement sur faille: cas vécu, mécanisme, remèdes, conséquence. *In* Maury, V.M., and Fourmaintraux, D. (Eds.), *Rock at Great Depth (Vol. 2):* Rotterdam (Balkema), 871–883.

Maury, V.M., and Zurdo, C., 1996. Drilling-induced lateral shift: a common cause of borehole collapse. *SPE pap.*

Moos, D., and Morin, R.H., 1991. Observations of wellbore failure in the Toa Baja well—implication for the state of stress in the North Coast Tertiary Basin, Puerto Rico. *Geophys. Res. Lett.*, 18:505–508.

Moos, D., and Zoback, M.D., 1990. Utilization of observations of well bore failure to constrain the orientation and magnitude of crustal stresses: application to continental, Deep Sea Drilling Project, and Ocean Drilling Program boreholes. *J. Geophys. Res.*, 95:9305–9325.

Plumb, R.A., and Hickman, S.H., 1985. Stress-induced borehole elongation: a comparison between the four-arm dipmeter and the borehole televiewer in the Auburn geothermal well. *J. Geophys. Res.*, 90:5513–5521.

Sibson, R.H., 1974. Frictional constraints on thrust, wrench, and normal faults. *Nature*, 249:542–544.

Tajima, F., and Célérier, B., 1989. Possible focal mechanism change during reactivation of a previously ruptured subduction zone. *Geophys. J. Int.*, 98:301–316.

Zoback, M.D., Moos, D., Mastin, L., and Anderson, R.N., 1985. Well bore breakouts and in situ stress. *J. Geophys. Res.*, 90:5523–5530.

Zoback, M.D., Zoback, M.L., et al., 1989. Global patterns of intraplate stress: a status report on the world stress map project of the International Lithosphere Program. *Nature*, 341:291–298.

Date of initial receipt: 27 May 1997
Date of acceptance: 28 January 1998
Ms 161SR-212

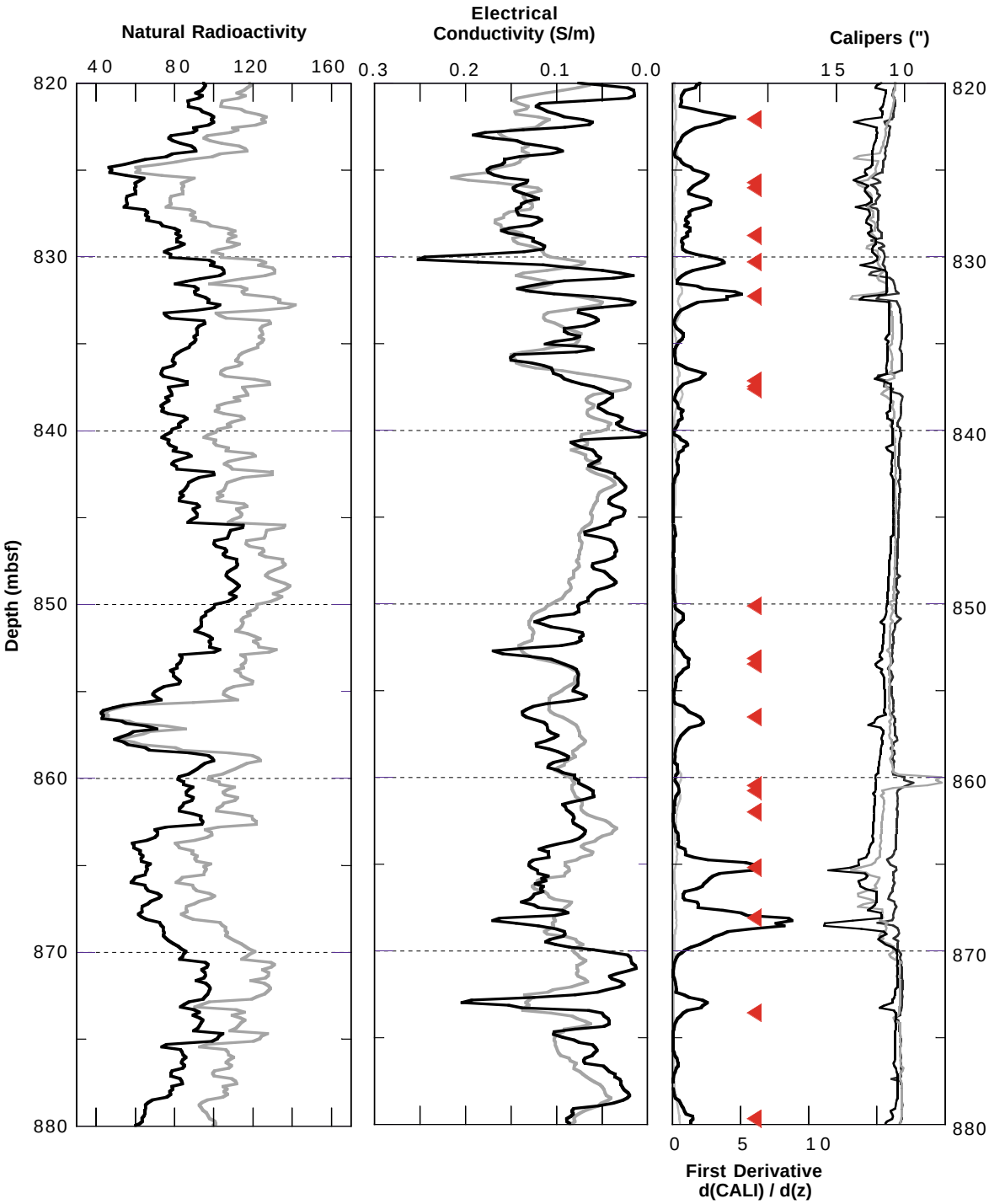

Figure 11. Detailed faulting analysis over 80 m in the lower basement section of Hole 976B, where the hole size is close to bit size (9.875 in). **Left:** Natural radioactivity traces (CGR in black and SGR in gray), with low values (e.g., 825 and 856 mbsf) in front of long-lived faults. **Center:** Electrical conductivity from Spherically Focused Log SFL (black) and induction deep measurements (gray). High values are expected from increased fracturing and porosity in front of faulted intervals. **Right:** Caliper measurements and first derivative of the density tool caliper (black). The location of the 20 faults with horizontal displacement identified from BHTV images is indicated with a triangle.

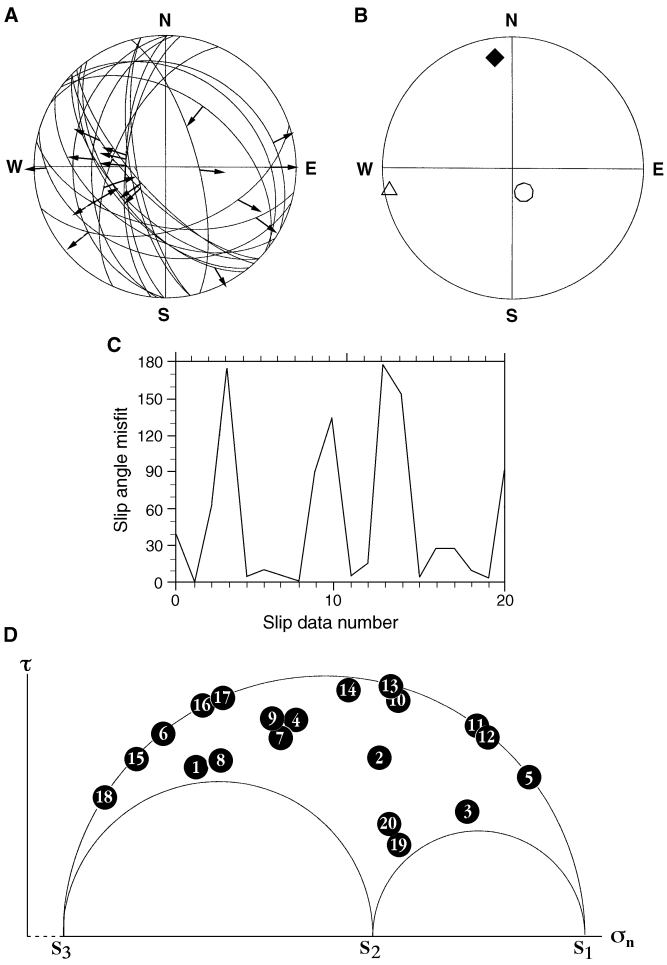

Figure 12. **A.** Lower hemisphere representation of the 20 fault planes mapped from BHTV data in Hole 976B. Inward and outward arrows correspond to normal and reverse faulting, respectively. **B.** Stress tensor derived from the inversion of the 20 fault planes and slip directions; $r_0 = (S_1–S_2) / (S_1–S_3)$. **C.** Angular difference between observed slip rake and that predicted by the solution stress tensor. **D.** Representation of each of the 20 fault planes in Mohr circles (adimensionalized as in Célérier, 1988).

Table 1. Fault characteristics and measurements of displacements using BHTV images, Hole 976B.

Fault	Depth (mbsf)	Slip direction (°)	Horizontal slip (cm)	Slip along fault plane (cm)	Plunge direction (°)	Fault dip (°)	Faulting mode
1	822.1	57	0.96	3.09	227.5	72	N
2	825.8	64	1.12	1.61	213.1	46	N
3	826.1	89	1.09	1.28	195.8	32	N-S
4	828.8	71	0.82	1.39	230.4	54	S
5	830.3	77	1.29	1.41	028.8	24	N-S
6	832.3	88	0.93	2.48	259.2	68	N
7	837.1	96	0.82	1.54	224.6	58	N
8	837.4	112	0.89	2.48	224.6	69	N
9	837.6	154	0.64	1.14	233.3	56	N
10	850.1	31	0.89	1.24	037.4	45	D
11	853.2	90	0.58	0.66	040.3	30	D
12	853.5	50	0.89	1.01	270.7	30	N
13	856.5	63	1.06	1.44	273.6	43	D
14	860.5	99	0.83	1.52	293.8	57	D
15	860.7	50	1.24	4.01	259.2	72	N
16	862.0	107	1.11	2.64	270.7	65	N-D
17	865.2	100	0.93	2.22	276.5	65	N-D
18	868.1	96	0.91	2.66	074.9	70	N
19	873.2	114	1.44	2.23	161.3	50	S
20	879.7	119	0.68	1.09	191.0	52	N

Notes: Depth interval = 820.0-880.0 mbsf. Faulting mode: N = normal fault, S = sinistral strike-slip, D = dextral strike-slip.

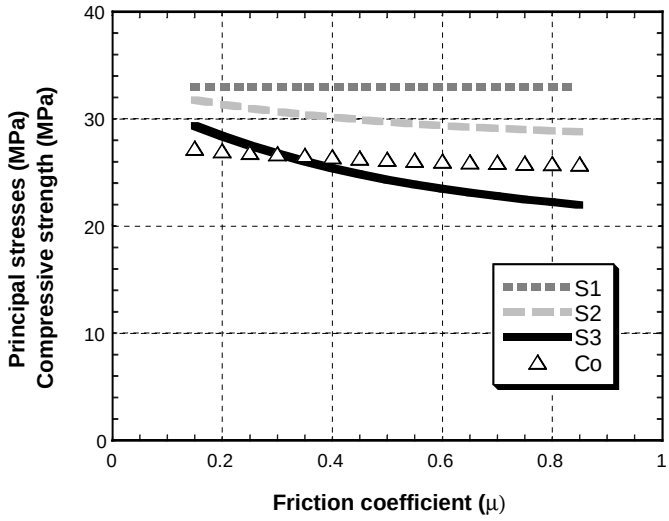

Figure 13. Principal stress magnitudes and compressive strength of the rock as a function of friction coefficient μ. S_1 = maximum (vertical) stress value; S_2 = horizontal maximum stress value; S_3 = horizontal minimum stress value; C_0 = mean computed compressive strength of the rock.